J. Fluid Mech. (2009), *vol.* 632, *pp.* 199–225. © 2009 Cambridge University Press
doi:10.1017/S0022112009006429 Printed in the United Kingdom

Axisymmetric and non-axisymmetric instability of an electrified viscous coaxial jet

FANG LI†, XIE-YUAN YIN AND XIE-ZHEN YIN

Department of Modern Mechanics, University of Science and Technology of China, Hefei, Anhui 230027, People's Republic of China

(Received 1 April 2008 and in revised form 21 January 2009)

A linear study is carried out for the axisymmetric and non-axisymmetric instability of a viscous coaxial jet in a radial electric field. The outer liquid is considered to be a leaky dielectric and the inner a perfect dielectric. The generalized eigenvalue problem is solved and the growth rate of disturbance is obtained by using Chebyshev spectral collocation method. The effects of the radial electric field, liquid viscosity, surface tension as well as other parameters on the instability of the jet are investigated. The radial electric field is found to have a strong destabilizing effect on non-axisymmetric modes, especially those having smaller azimuthal wavenumbers. The helical mode becomes prevalent over other modes when the electric field is sufficiently large. Non-axisymmetric modes with high azimuthal wavenumbers may be the most unstable at zero wavenumber. Liquid viscosity has a strong stabilizing effect on both the axisymmetric and non-axisymmetric instability. Relatively, the helical instability is less suppressed and therefore becomes predominant at high liquid viscosity. Surface tension promotes the instability of the para-sinuous mode and meanwhile suppresses the helical and the other non-axisymmetric modes in long wavelength region.

1. Introduction

In coaxial electrospraying and coaxial electrospinning experiments, two immiscible liquids are emitted from two homocentric capillary tubes, respectively. Under certain condition, a stationary double-layer Taylor cone is formed, with a coaxial jet ejected from the tip of the cone. The coaxial jet is inherently unstable. It may undergo different instability modes owing to the imposed electric field, for example, breaking up into compound droplets (referred as coaxial electrospraying) or whipping in three-dimensional space (coaxial electrospinning) (Loscertales *et al.* 2002; López-Herrera *et al.* 2003; Sun *et al.* 2003; Yu, Fridrikh & Rutledge 2004; Chen *et al.* 2005). Coaxial electrospraying and coaxial electrospinning are effective methods to produce micro/nano capsules and composite ultrafine fibres that have a variety of applications in drug industry, food additives, material engineering and so on.

Theoretically, the behaviour of a coaxial jet is associated closely with the instability characteristic of the jet. When a coaxial jet is perturbed by an arbitrary infinitesimal disturbance, its inner and outer interfaces will be modulated. In the cylindrical coordinate system (r, θ, z) where r, θ, z are, respectively, the radial, azimuthal and axial coordinates, the disturbance can be decomposed into Fourier exponential of

† Email address for correspondence: fli6@ustc.edu.cn

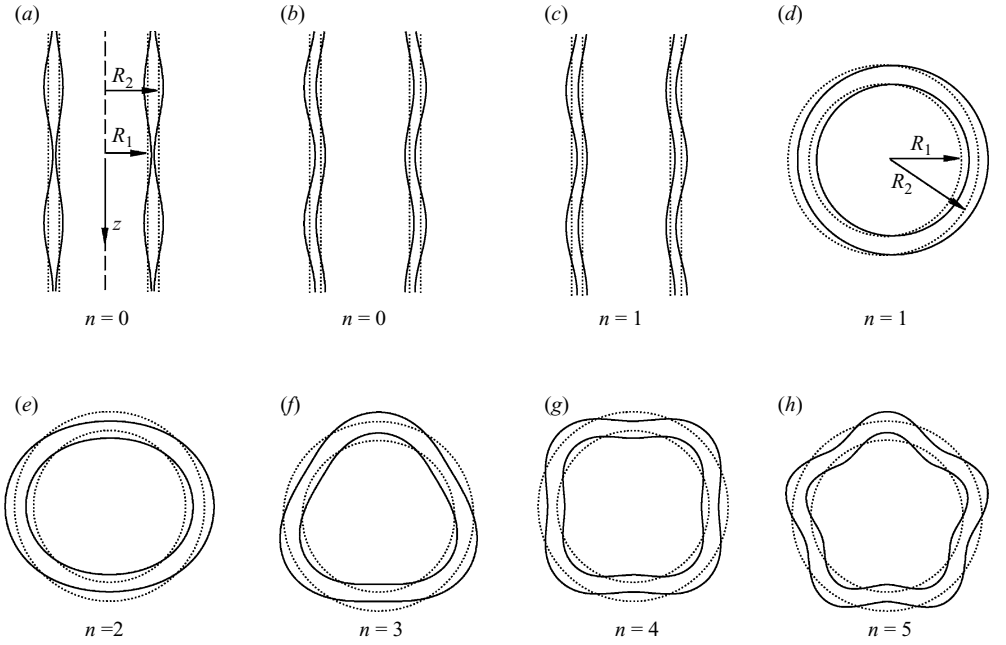

FIGURE 1. Sketch of the unstable modes. (*a*) The para-varicose mode, (*b*) the para-sinuous mode, (*c*) and (*d*) the helical mode (*e*) the non-axisymmetric mode $n = 2$, (*f*) the non-axisymmetric mode $n = 3$, (*g*) the non-axisymmetric mode $n = 4$ and (*h*) the non-axisymmetric mode $n = 5$. Solid curves: the interfaces after perturbed; dotted curves: the interfaces before perturbed.

the form $e^{\omega t + i(kz + n\theta)}$, where ω is the complex growth rate in temporal instability analysis, t is the time, $i = \sqrt{-1}$ is the imaginary unit, k is the real axial wavenumber and n is the azimuthal wavenumber (integer). According to the phase difference of the perturbations at the inner and outer interfaces, there exist two unstable modes, i.e. para-varicose mode and para-sinuous mode, for the axisymmetric instability ($n = 0$). The corresponding interface deformation in the r–z plane is sketched in figures 1(*a*) and 1(*b*). For para-varicose mode the interfaces are perturbed almost out of phase, while for para-sinuous mode the interfaces are deformed in phase. For non-axisymmetric instability of a certain azimuthal wavenumber n, there exists only one unstable mode. The interface configurations of several non-axisymmetric instability modes with small azimuthal wavenumbers ($n = 1$, 2, 3, 4, 5) are shown in figures 1(*c*)–1(*h*), respectively. For the non-axisymmetric mode $n = 1$, also called the helical mode, the interfaces and the central line of the jet are displaced in phase with the area of cross-section unchanged, as sketched in figures 1(*c*) and 1(*d*). For the non-axisymmetric modes $n = 2$, 3, 4 and 5, the central line of the jet is unperturbed, but the periodical variation of the interfaces arises in the r–θ plane, the period of which is determined by the value of n. The non-axisymmetric modes may lead to the formation of irregular ramified shapes during the breakup process of the jet (Hartman *et al.* 2000). For a single liquid jet a non-axisymmetric mode with relatively small azimuthal wavenumber is easier to destabilize (Avital 1995). The same phenomenon is found in the coaxial jet case.

In coaxial electrospraying, axisymmetric disturbances dominate in the breakup process and the jet therefore breaks up into compound droplets. However, helical

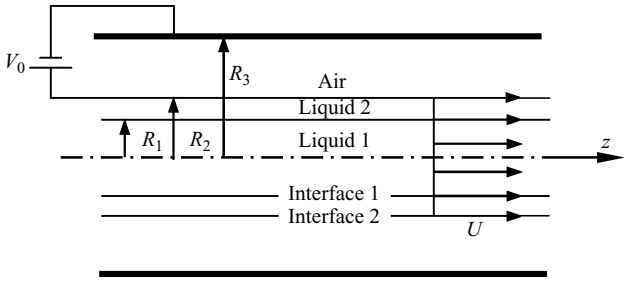

FIGURE 2. Schematic description of the theoretical model.

instability predominates over axisymmetric instability in coaxial electrospinning, leading to the bending of the jet in space without breakup. The authors developed a leaky dielectric model to study the axisymmetric instability of a viscous coaxial jet in a radial electric field (Li, Yin & Yin 2008*a*). The analytical dispersion relations were derived and the temporal growth rates of the unstable modes were solved. The effects of the radial electric field as well as the other parameters on the jet instability were discussed in detail. In our recent paper (Li, Yin & Yin 2008*b*), the helical instability was compared with the axisymmetric instability briefly. Both the radial and axial electric fields were found to have remarkable effects on them. However, a comprehensive comparison between axisymmetric and non-axisymmetric instability remains to be implemented. In the present paper we will research all possible unstable modes in the outer-driving coaxial jet case. A theoretical model similar to that established in Li *et al.* (2008*a*) is used. We aim to gain some insight into the effects of the radial electric field as well as physical properties of the jet on axisymmetric and non-axisymmetric instability, and seek the condition that favours the predominance of the desirable modes.

The paper is organized as follows: In § 2, the theoretical model is described. The basic velocity profile is simplified appropriately. The governing equations and boundary conditions are given. In § 3, the complex eigenvalue is calculated numerically. The effects of the radial electric field and physical properties of the liquids on the growth rates of the axisymmetric and non-axisymmetric modes are investigated. Particularly, the effect of liquid viscosity on the predominance of the para-sinuous and helical modes is discussed. In § 4, the main conclusions are drawn.

2. Theoretical model

Consider an infinitely long coaxial cylindrical jet consisting of two liquids, as sketched in figure 2. The radii of the inner and outer liquids are R_1 and R_2, respectively. An annular electrode of radius R_3 is positioned around the jet. An electrical potential V_0 is imposed between the outer interface of the jet and the electrode. The medium between the electrode and the jet is air under normal condition. In the outer-driving coaxial jet case, the outer liquid is considered to be a leaky dielectric of finite conductivity, acting as driving liquid. The conductivities of the inner liquid and ambient air are so small that they are considered to be perfect dielectrics. The conductivity of the outer liquid is assumed to be large enough for free charge to relax to the outer interface of the jet. There is no charge in the jet (Higuera 2007; Li *et al.* 2008*a*). In the unperturbed state, free charge is distributed on the outer

interface uniformly, with zero basic electric field in the jet. The electric field intensity in the air is $-V_0/[r\ln(R_2/R_3)]$ in the radial direction, where 'ln' stands for the natural logarithm. The density of charge is $-\varepsilon_3 V_0/[R_2\ln(R_2/R_3)]$, where ε_3 is the electrical permittivity of the air.

The liquids are assumed to be incompressible viscous fluids. There is no mass transfer at the interfaces. The effects of gravity, magnetic field and temperature are neglected. The jet before perturbed is assumed to be cylindrical. The basic flow is steady and axisymmetric. In the cylindrical coordinates (r, θ, z) the basic velocity only has the non-zero component in the axial direction, i.e.

$$\boldsymbol{U}_m = (U_{mr}, U_{m\theta}, U_{mz}) = (0, 0, U_{mz}(r)), m = 1, 2, 3 \tag{2.1}$$

where the subscripts 1, 2 and 3 stand for the inner liquid, the outer liquid and the air, respectively. The velocity components $U_{mz}(r)$ satisfying the steady momentum equation and boundary conditions are (Li *et al.* 2008*a*)

$$U_{1z} = 1 + \mu_{r3}\frac{1-a^2}{b^2-1} + \frac{\mu_{r3}}{\mu_r}\frac{a^2-r^2}{b^2-1}, \tag{2.2a}$$

$$U_{2z} = 1 + \mu_{r3}\frac{1-r^2}{b^2-1}, \tag{2.2b}$$

$$U_{3z} = \frac{b^2-r^2}{b^2-1}, \tag{2.2c}$$

where the velocity components are scaled by the velocity at the outer interface of the jet, $a = R_1/R_2$ and $b = R_3/R_2$ are the radius ratios, $\mu_r = \mu_1/\mu_2$ is the viscosity of the inner liquid relative to the outer liquid, and $\mu_{r3} = \mu_3/\mu_2$ is the viscosity of the air relative to the outer liquid. It is supposed that the viscosity of the air is much smaller than that of the liquids, i.e. $\mu_{r3} \ll 1$. In such a case we have $U_{1z} \approx 1$ and $U_{2z} \approx 1$. That is, the velocities of the inner and outer liquids are equal and constant. Furthermore, we assume that the hydrodynamic effect of the air is negligible in the instability analysis. Therefore, it is convenient to apply a relative coordinate system moving with the jet. In addition, the radius of the annular electrode is supposed to be much larger than that of the jet, i.e. $b \gg 1$. The assumption is appropriate for most electrified coaxial jet experiments.

The driving pressure gradients in the liquids and air, $\partial P_m/\partial z$, where P_m is the basic pressure field, must be equal in order to meet force balance at the interfaces (Chen & Lin 2002). The pressure fields of the liquids and air have the following relationships:

$$P_1 = P_2 + \frac{\gamma_1}{R_1}, \quad P_3 = P_2 - \frac{\gamma_2}{R_2} + \frac{\varepsilon_3 V_0^2}{2R_2^2\ln^2(R_2/R_3)},$$

where γ_j, $j = 1, 2$, is the surface tension coefficient. Hereafter, the subscripts 1 and 2 stand for the inner interface and the outer interface, respectively, while referring to the quantities on the interfaces. Although the radial electric field affects force balance in the unperturbed state, it has no effect on the basic velocity profile owing to the absence of electrical shear stresses.

When the jet is disturbed, the perturbations of all the quantities are assumed to be small. The small disturbance assumption allows us to expand the governing equations and boundary conditions and only keep the linear terms in the linear instability analysis. Choosing ρ_2, R_2, U (the velocity of the jet) and $\rho_2 U^2$ as the characteristic density, length, velocity and pressure, we non-dimensionalize the equations. The

governing equations linearized in the dimensionless form are

$$\nabla \cdot \boldsymbol{u}_{1,2} = 0, \tag{2.3}$$

$$\frac{\partial \boldsymbol{u}_1}{\partial t} = -\frac{1}{S}\nabla p_1 + \frac{\mu_r}{SRe}\nabla^2 \boldsymbol{u}_1, \tag{2.4}$$

$$\frac{\partial \boldsymbol{u}_2}{\partial t} = -\nabla p_2 + \frac{1}{Re}\nabla^2 \boldsymbol{u}_2, \tag{2.5}$$

where $\boldsymbol{u}$ and p are the perturbations of the velocity and pressure, respectively. $S = \rho_1/\rho_2$ is the density ratio of the inner to the outer liquid and $Re = \rho_2 U R_2/\mu_2$ is the Reynolds number.

The three components of the velocity and the pressure at the symmetry axis $r = 0$ satisfy the following consistency conditions (Ash & Khorrami 1995):

$$u_{1r} = u_{1\theta} = \frac{\partial u_{1z}}{\partial r} = \frac{\partial p_1}{\partial r} = 0 \quad \text{for} \quad n = 0, \tag{2.6}$$

$$u_{1z} = p_1 = 0, \quad u_{1r} + \frac{\partial u_{1\theta}}{\partial \theta} = 0, \quad 2\frac{\partial u_{1r}}{\partial r} + \frac{\partial^2 u_{1\theta}}{\partial r \partial \theta} = 0 \quad \text{for} \quad n = 1, \tag{2.7}$$

$$u_{1r} = u_{1\theta} = u_{1z} = p_1 = 0 \quad \text{for} \quad n > 1. \tag{2.8}$$

At the inner interface $r = a + \eta_1$, the kinematic boundary condition, the continuity of the velocity and the balance of forces in two tangential and one normal directions should be satisfied, i.e.

$$u_{1r} = \frac{\partial \eta_1}{\partial t}, \tag{2.9}$$

$$\boldsymbol{u}_1 = \boldsymbol{u}_2, \tag{2.10}$$

$$\frac{1}{Re}\left(\frac{\partial u_{2r}}{\partial z} + \frac{\partial u_{2z}}{\partial r}\right) - \frac{\mu_r}{Re}\left(\frac{\partial u_{1r}}{\partial z} + \frac{\partial u_{1z}}{\partial r}\right) = 0, \tag{2.11}$$

$$\frac{1}{Re}\left(\frac{\partial u_{2r}}{r\partial \theta} + \frac{\partial u_{2\theta}}{\partial r} - \frac{u_{2\theta}}{r}\right) - \frac{\mu_r}{Re}\left(\frac{\partial u_{1r}}{r\partial \theta} + \frac{\partial u_{1\theta}}{\partial r} - \frac{u_{1\theta}}{r}\right) = 0, \tag{2.12}$$

$$p_1 - \frac{2\mu_r}{Re}\frac{\partial u_{1r}}{\partial r} - p_2 + \frac{2}{Re}\frac{\partial u_{2r}}{\partial r} = \frac{\Gamma}{We}\nabla \cdot \boldsymbol{n}_1; \tag{2.13}$$

at the outer interface $r = 1 + \eta_2$, the kinematic boundary condition and the balance of forces in the tangential and normal directions should be satisfied, i.e.

$$u_{2r} = \frac{\partial \eta_2}{\partial t}, \tag{2.14}$$

$$\frac{1}{Re}\left(\frac{\partial u_{2r}}{\partial z} + \frac{\partial u_{2z}}{\partial r}\right) - \zeta E_{3z} + \zeta n_{2z} = 0, \tag{2.15}$$

$$\frac{1}{Re}\left(\frac{\partial u_{2r}}{r\partial \theta} + \frac{\partial u_{2\theta}}{\partial r} - \frac{u_{2\theta}}{r}\right) - \zeta E_{3\theta} + \zeta n_{2\theta} = 0, \tag{2.16}$$

$$p_2 - \frac{2}{Re}\frac{\partial u_{2r}}{\partial r} + \frac{1}{2}\zeta E_{3r}^2 = \frac{1}{We}\nabla \cdot \boldsymbol{n}_2, \tag{2.17}$$

where η_j, $j=1$, 2, is the displacement of the interface from its equilibrium position R_j, $\boldsymbol{n}_j$ is the outward normal unit vector on the interface, E is the component of the electric field intensity, $We=\rho_2 U^2 R_2/\gamma_2$ is the Weber number representing the magnitude of the surface tension relative to the inertial force, $\zeta=\varepsilon_3 V_0^2/\rho_2 U^2 R_2^2 \ln^2(R_2/R_3)$ is the electrical Euler number representing the magnitude of the electrical stress relative to the inertial force and $\Gamma=\gamma_1/\gamma_2$ is the interface tension coefficient ratio of the inner and outer interfaces. The components of $\boldsymbol{n}$ and the corresponding curvature of the interface are, respectively,

$$\boldsymbol{n}=(n_r, n_\theta, n_z)=\left(1, -\frac{\partial \eta}{r\partial\theta}, -\frac{\partial \eta}{\partial z}\right) \quad \text{and} \quad \nabla\cdot\boldsymbol{n}=\frac{1}{r}-\frac{1}{r^2}\frac{\partial^2\eta}{\partial\theta^2}-\frac{\partial^2\eta}{\partial z^2}.$$

It can be seen from (2.11)–(2.13) that there is no electric field contribution to the force balance at the inner interface. This is because that the electrical stresses at the inner interface are high-order quantities. They are ignored in the linear scope. Electrical stresses only appear in the force balance conditions at the outer interface.

In electrostatics the electrical potential perturbation ψ_m satisfies the Laplace equation

$$\nabla^2\psi_m=0, m=1, 2, 3 \tag{2.18}$$

with the electric field intensity $\boldsymbol{E}_m=-\nabla\psi_m$.

The electric field must be bounded at the symmetry axis $r=0$. At the inner interface $r=a+\eta_1$, the continuity of the tangential electric field and the normal electric displacement should be satisfied, i.e.

$$\boldsymbol{n}_1\times(\boldsymbol{E}_2-\boldsymbol{E}_1)=0, \tag{2.19}$$

$$\boldsymbol{n}_1\cdot(\varepsilon_{r2}\boldsymbol{E}_2-\varepsilon_{r1}\boldsymbol{E}_1)=0; \tag{2.20}$$

at the outer interface $r=1+\eta_2$, the continuity of the tangential electric field, the Gauss law and the interface charge conservation equation should be satisfied (Melcher & Taylor 1969; Saville 1997), i.e.

$$\boldsymbol{n}_2\times(\boldsymbol{E}_3-\boldsymbol{E}_2)=0, \tag{2.21}$$

$$\boldsymbol{n}_2\cdot(\boldsymbol{E}_3-\varepsilon_{r2}\boldsymbol{E}_2)=q_s, \tag{2.22}$$

$$\frac{\partial q_s}{\partial t}-\boldsymbol{n}_2\cdot(\boldsymbol{n}_2\cdot\nabla)\boldsymbol{u}_2-\tau\varepsilon_{r2}\boldsymbol{E}_2\cdot\boldsymbol{n}_2=0, \tag{2.23}$$

where q_s is the perturbation of the dimensionless charge density at the outer interface. The relevant dimensionless parameters are the relative electrical permittivity of the inner liquid $\varepsilon_{r1}=\varepsilon_1/\varepsilon_3$, the relative electrical permittivity of the outer liquid $\varepsilon_{r2}=\varepsilon_2/\varepsilon_3$ and the relative electrical relaxation time $\tau=R_2\sigma_2/U\varepsilon_2$, where σ_2 is the electrical conductivity of the outer liquid.

Substituting the Fourier decomposition into (2.3)–(2.23), we obtain a set of the ordinary differential equations of eigenfunctions. The equations are written in a condensed form in the Appendix.

3. Numerical results and discussion

In this section we analyse the temporal instability of the electrified coaxial jet. Since in the theoretical model the basic velocity profile is simplified to be uniform, it is possible to derive the analytical dispersion relations for the axisymmetric and non-axisymmetric instability. For the axisymmetric instability, the dispersion relation

$D(k, \omega) = 0$ as well as the amplitude ratio of the interface perturbations $\hat{\eta}_1/\hat{\eta}_2$ has the similar form to that derived in Li *et al.* (2008*a*). For the non-axisymmetric instability, the analytical dispersion relation will be far more complicated. So we solve the problem using numerical method. For the problem formulated in the Appendix, the complex growth rate ω can be obtained numerically by means of the Chebyshev spectral collocation method. The procedure is outlined as follows. First, the radial coordinate r is transformed to the calculation space $y \in [-1, 1]$. Considering the velocity profile of the jet is uniform, a linear transform is appropriate. For the inner liquid domain $r \in [0, a]$, the transform is

$$r = \frac{a(1+y)}{2};$$

for the outer liquid domain $r \in [a, 1]$, the transform is

$$r = \frac{(a-1)y + 1 + a}{2}.$$

In the bounded domain $y \in [-1, 1]$, the bulk eigenfunctions and their derivatives are expanded in Chebyshev series. Then the governing equations in bulk are evaluated at the Gauss–Lobatto collocation points $y_j = \cos(j\pi/N)$, $j = 0, 1, \ldots, N$, where N is the number of the collocation points. At the interfaces and the symmetry axis the corresponding boundary conditions are evaluated. Finally the problem turns into a generalized eigenvalue problem of the same form as in the Appendix. In order to ensure convergence, the number of the collocation points in the inner liquid (N_1) is commonly 10–15, and in the outer liquid (N_2) it is 5–10. The number of the expansion coefficients of Chebyshev series is $4N_1 + 4N_2 + 11$. The size of matrices $\boldsymbol{A}$ and $\boldsymbol{B}$ after discretization is $(4N_1 + 4N_2 + 11) \times (4N_1 + 4N_2 + 11)$. A MATLAB code is developed to solve the generalized eigenvalue problem. The validity of the code has been examined by the result in Li *et al.* (2008*a*).

As mentioned above, for axisymmetric instability of a coaxial jet there are two unstable modes, i.e. the para-sinuous and the para-varicose modes, in the Rayleigh regime (in this regime the jet breaks up into droplets of diameter comparable to jet diameter, i.e. the dimensionless axial wavenumber k is of the order of unity) (Lin 2003). In most situations, the para-sinuous mode is much more unstable than the para-varicose mode and therefore dominates in the jet instability. This is the case of coaxial electrospraying (Loscertales *et al.* 2002; López-Herrera *et al.* 2003; Chen *et al.* 2005). While the helical instability becomes dominant, the jet produces not microcapsules but composite ultrafine fibres. This corresponds to the case of coaxial electrospinning (Sun *et al.* 2003; Yu *et al.* 2004). In practical applications the products of coaxial electrospraying and coaxial electrospinning are expected to be monodisperse. To realize it, we need to promote the destabilization of the desirable mode and at the same time suppress the instability of all the other modes. Here we aim to discover the condition that favours the predominance of the para-sinuous mode and the helical mode.

In the outer-driving electrified coaxial jet case, we take water and sunflower oil as the outer and inner liquids, respectively. Water is a leaky dielectric of finite conductivity. Sunflower oil is a perfect dielectric of negligible conductivity. The physical properties of them can be found in López-Herrera *et al.* (2003). In order to be more close to experimental situations, we assume that the jet diameter is of the order of micrometres. The velocity of the jet is about 1 m s^{-1}. The electrical potential between the jet surface and the electrode is several thousand volts, and

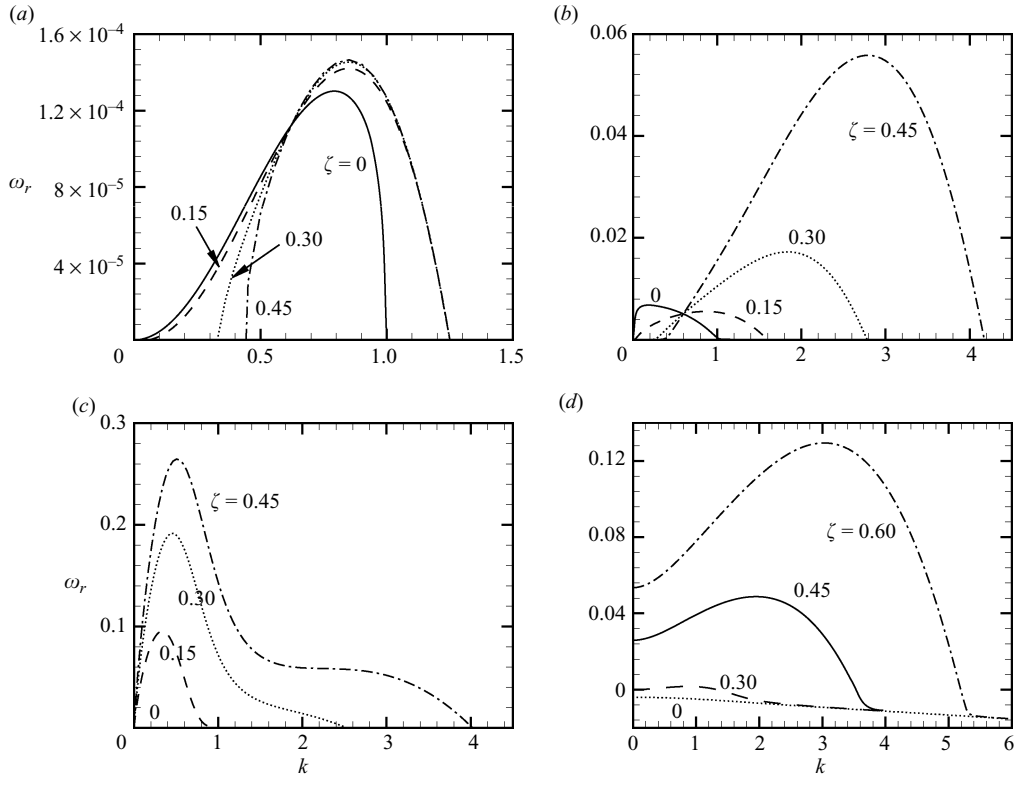

FIGURE 3. The effect of the radial electric field on the growth rates of (*a*) the para-varicose mode $n=0$, (*b*) the para-sinuous mode $n=0$, (*c*) the helical mode $n=1$ and (*d*) the non-axisymmetric mode $n=2$.

the radius of the electrode is of the order of centimetres. Based on the assumption as above we can estimate value ranges of the dimensionless parameters. There are 10 dimensionless parameters in this problem. For convenience of calculation and comparison, a reference state is supposed. The reference dimensionless parameters are $S=0.84$, $a=0.8$, $\mu_r=43$, $Re=10$, $We=10$, $\Gamma=0.23$, $\zeta=0.15$, $\varepsilon_{r1}=3.4$, $\varepsilon_{r2}=80$ and $\tau=1$. In the calculation the dimensionless parameters are fixed to the reference values unless stated otherwise.

3.1. *Effect of the radial electric field on the jet instability*

The effect of the radial electric field on the para-varicose mode and para-sinuous mode is represented in figures 3(*a*) and 3(*b*), respectively. It is shown that the radial electric field has a two-fold effect on the two modes: at wavenumbers smaller than a certain value, the electric field suppresses the instability of the modes; at wavenumbers larger than the value, the electric field enhances the instability of them. The growth rate of the para-varicose mode is usually three orders of magnitude smaller than that of the para-sinuous mode. The effect of the electric field on the para-sinuous mode is more profound. As the electrical Euler number ζ increases, the waves in long wavelength region become less unstable, and moreover, the most possible wavenumber k_{max} corresponding to the maximum growth rate ω_{max} together with the cut-off wavenumber k_c moves towards short wavelength region. Accordingly the coaxial jet breaks up into droplets of diameter smaller than those at zero electric

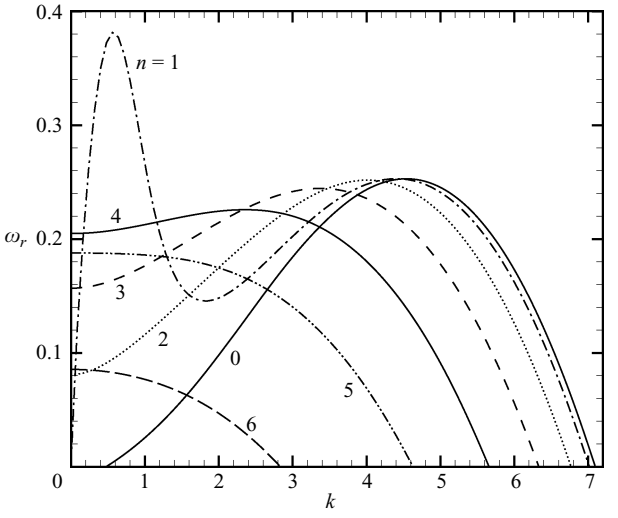

FIGURE 4. Comparison of the growth rates of the para-sinuous mode and the unstable non-axisymmetric modes. $\zeta = 0.75$.

field. The electric field may accelerate the breakup of the jet significantly in short wavelength region.

In the absence of electric field, the helical mode and the other non-axisymmetric modes are stable. The radial electric field turns out to be the only factor in this problem that results in the instability of the non-axisymmetric modes. As the electric field increases, they become unstable one by one. The non-axisymmetric mode with relatively small azimuthal wavenumber is easier to be destabilized. Figures 3(*c*) and 3(*d*) illustrate the effect of the radial electric field on the growth rates of the helical mode and the non-axisymmetric mode $n = 2$, respectively. Apparently, the electric field has a strong destabilizing effect on them. The most possible wavenumber of the helical mode locates in long wavelength region. As ζ increases, k_{max} is enlarged to a certain extent. In addition, the electric field makes the waves in relatively short wavelength region unstable, but their growth rates are smaller compared to the maximum growth rate. For the non-axisymmetric mode $n = 2$, k_{max} appears near zero when the electric field is small. As ζ increases, k_{max} and k_c move towards short wavelength region. The calculation result shows that the effect of the radial electric field on the non-axisymmetric modes $n > 2$ is similar to that on $n = 2$, which is not plotted here.

To compare the axisymmetric and non-axisymmetric instability further, the growth rates of the para-sinuous and non-axisymmetric modes are plotted in figure 4, where the electrical Euler number is fixed at a relatively large value, i.e. $\zeta = 0.75$. The non-axisymmetric modes up to $n = 6$ are unstable. At zero axial wavenumber, the non-axisymmetric mode $n = 4$ is the most unstable. The other non-axisymmetric modes $n = 2$, 3, 5, 6 also have non-zero growth rates. The phenomenon indicates that the ramified jet breakup may occur if an infinitely long-wave perturbation is imposed on the jet compulsively. In long wavelength region, the growth rate of the helical mode is the largest, and therefore the helical mode dominates. In relatively small wavelength region, the para-sinuous mode is the most unstable. However, when the electric field is sufficiently strong, as illustrated in figure 4, the growth rates of the non-axisymmetric modes become comparable to that of the para-sinuous mode.

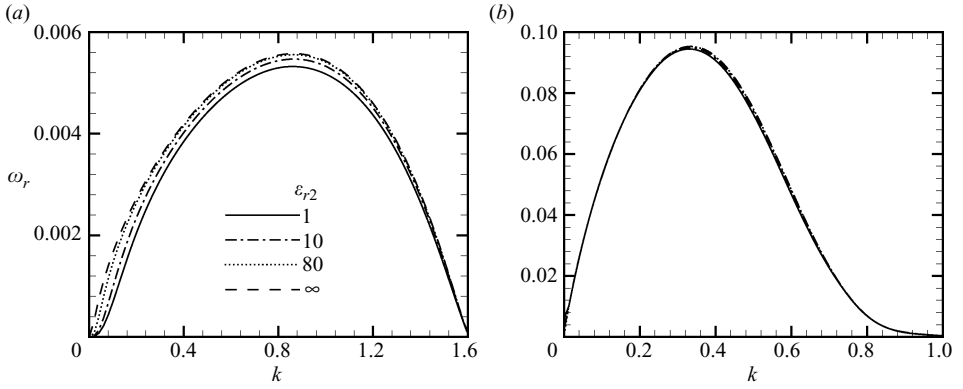

FIGURE 5. The effect of the relative electrical permittivity of the outer liquid on the growth rates of (*a*) the para-sinuous mode $n=0$ and (*b*) the helical mode $n=1$.

Moreover, the most possible wavenumbers of them are close to each other. In such a case it is hard to discern which is dominant.

In general, the helical mode is the most unstable instead of the para-sinuous mode, when the radial electric field is amplified sufficiently. At large electric field, the para-sinuous mode, helical mode and even non-axisymmetric modes with higher azimuthal wavenumbers have equal opportunity to be destabilized in short wavelength region. From this point large electric field is undesirable for the predominance of the para-sinuous mode. At zero axial wavenumber, non-axisymmetric instability is dominant, the details of which are determined by the magnitude of the electric field strength.

3.2. *Effect of the electrical properties of the liquids on the jet instability*

In the leaky dielectric model, the relative electrical permittivities of the inner and outer liquids, i.e. ε_{r1} and ε_{r2}, are involved. Mathematically, it can be seen from matrix $\boldsymbol{A}$ in the Appendix that the effect of them on the jet instability seems complicated. Here we perform a brief analysis within typical value range. Figures 5(*a*) and 5(*b*) illustrate the effect of ε_{r2} on the growth rates of the para-sinuous mode and helical mode, respectively. (The para-varicose mode is much less unstable than the para-sinuous mode and helical mode, and the non-axisymmetric modes $n>2$ are stable. The curves of them are not shown.) In the figure the maximum growth rate and corresponding most possible wavenumber change little, as ε_{r2} varies. Moreover, ε_{r2} has no influence on the cut-off wavenumber. It was found that the limit of $\varepsilon_{r2}\to\infty$ is equivalent to the case in which the outer-driving liquid has infinite electrical conductivity (Li *et al.* 2008*a*). In such a case the relative permittivities of the liquids as well as the relative electrical relaxation time are not involved in the instability analysis. In order to research the effect of ε_{r1}, we keep ε_{r2} at a small number, i.e. $\varepsilon_{r2}=3.4$. Figures 6(*a*) and 6(*b*) illustrate the effect of ε_{r1} on the growth rates of the para-sinuous mode and helical mode, respectively. It is shown that the permittivity of the inner liquid also has no significant effect on the instability of the unstable modes.

In this problem, there are several characteristic times. They are the electrical relaxation time $\tau_e\sim\varepsilon_2/\sigma_2$, the convective time $\tau_F\sim R_2/U$, the capillary time $\tau_c\sim(\rho_2R_2^3/\gamma_2)^{1/2}$ and the viscous diffusion time $\tau_v\sim\rho_2R_2^2/\mu_2$. Suppose $\rho_2=1000$ kg m^{-3}, $\mu_2=1.0\times10^{-3}$ kg m^{-1} s^{-1}, $\gamma_2=0.072$ N m^{-1}, $\varepsilon_2=80$ (relative to vacuum), $\sigma_2=4\times10^{-6}$ S m^{-1}, $R_2=10^{-5}$ m, $U=1$ m s^{-1}. The values of the characteristic times are $\tau_e\approx1.8\times10^{-4}$ s, $\tau_F\approx1.0\times10^{-5}$ s, $\tau_c\approx3.7\times10^{-6}$ s and $\tau_v\approx1.0\times10^{-4}$ s,

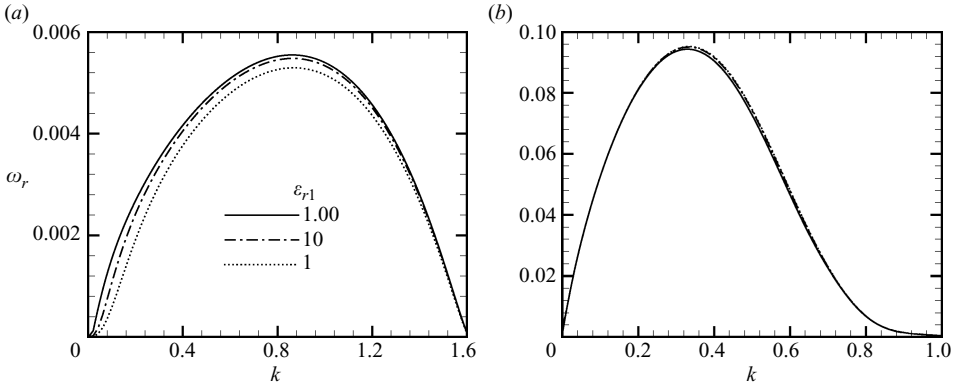

FIGURE 6. The effect of the relative electrical permittivity of the inner liquid on the growth rates of (*a*) the para-sinuous mode $n=0$ and (*b*) the helical mode $n=1$. $\varepsilon_{r2}=3.4$.

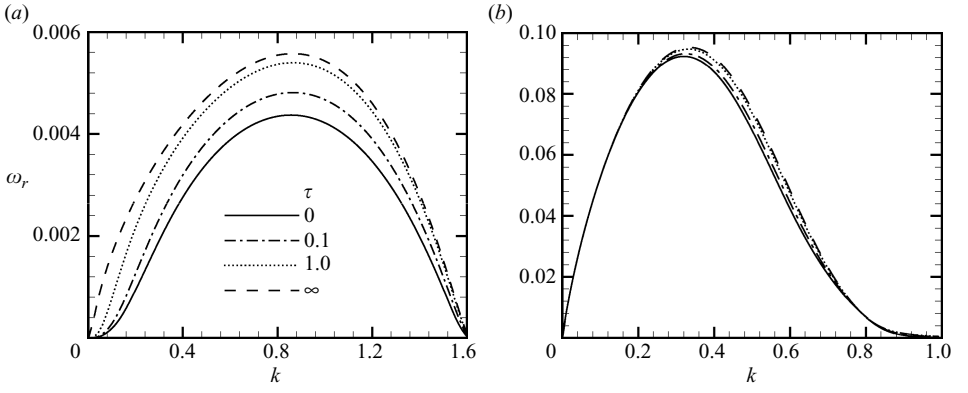

FIGURE 7. The effect of the relative electrical relaxation time on the growth rates of (*a*) the para-sinuous mode $n=0$ and (*b*) the helical mode $n=1$. $\varepsilon_{r2}=3.4$.

respectively. The estimation shows that none of the characteristic times can be far larger than the others. It indicates that the conduction, convection, capillary and viscosity are all important in this problem. We use the ratio of the convective time to the electrical relaxation time, i.e. $\tau = R_2\sigma_2/U\varepsilon_2$, to weigh the speed of free charge relaxation. If τ approaches zero, it corresponds to the large electrical relaxation time limit (LERT); conversely, if τ approaches infinity, it corresponds to the small electrical relaxation time limit (SERT) (Li *et al.* 2008*a*). Figures 7(*a*) and 7(*b*) illustrate the effect of τ on the growth rates of the para-sinuous mode and helical mode, respectively. For the same reason as mentioned earlier, the relative permittivity of the outer liquid ε_{r2} is kept at 3.4. For a fixed wavenumber, the SERT case is the most unstable, and the LERT case is the least unstable. However, similar to the electrical permittivities of the liquids, the electrical relaxation time influences the jet instability to a limited extent, particularly for the helical mode.

3.3. *Effect of the viscosity of the liquids on the jet instability*

3.3.1. *Effect of liquid viscosity*

In this model, two dimensionless parameters are related to liquid viscosity. They are the Reynolds number $Re = \rho_2 U R_2/\mu_2$ and the viscosity ratio $\mu_r = \mu_1/\mu_2$. The Reynolds number Re measures the magnitude of the viscosity of the outer liquid.

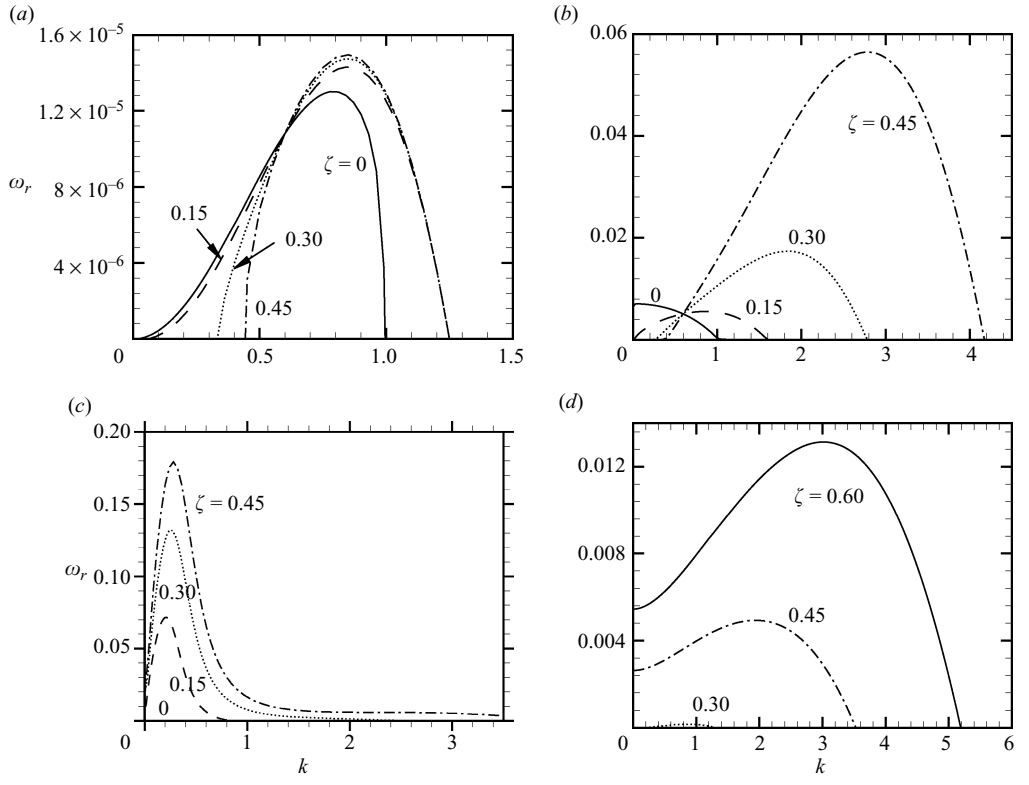

FIGURE 8. The effect of the radial electric field on the growth rates of (*a*) the para-varicose mode $n=0$, (*b*) the para-sinuous mode $n=0$, (*c*) the helical mode $n=1$ and (*d*) the non-axisymmetric mode $n=2$. $Re=1$.

The Reynolds number of the inner liquid is a combined dimensionless parameter, i.e. $Re_1=\rho_1 U R_2/\mu_1=SRe/\mu_r$. Apparently, Re_1 increases or decreases together with Re. Considering that the viscosity of the inner and outer liquids may have similar effect on the jet instability, we study the effect of liquid viscosity through changing the value of Re, leaving μ_r in the reference state.

Figures 8(*a*)–8(*d*) illustrate the growth rates of the para-varicose mode, para-sinuous mode, helical mode and non-axisymmetric mode $n=2$, respectively, at a relatively small Reynolds number $Re=1$. Compared with figure 3 where $Re=10$, it can be seen that all the modes are suppressed. For a fixed electrical Euler number ζ, the maximum growth rates of the para-varicose mode, para-sinuous mode and non-axisymmetric mode $n=2$ are decreased to about one tenth of that at $Re=10$. The helical mode is also decreased, but not so much as the others. The most possible wavenumbers of the modes move towards long wavelength region to a certain extent as the Reynolds number decreases. The Reynolds number has no influence on the cut-off wavenumbers of the modes.

The result in a relatively large electric field is shown in figure 9, where the electrical Euler number $\zeta=0.75$. In the figure the y-axis on the left side is for the para-sinuous mode and the non-axisymmetric modes $n>1$, and the y-axis on the right side is for the helical mode. The non-axisymmetric modes up to $n=6$ are unstable. Compared with the result in figure 4, the growth rates of the unstable modes except that of the helical one are decreased dramatically. The helical mode is stabilized a little.

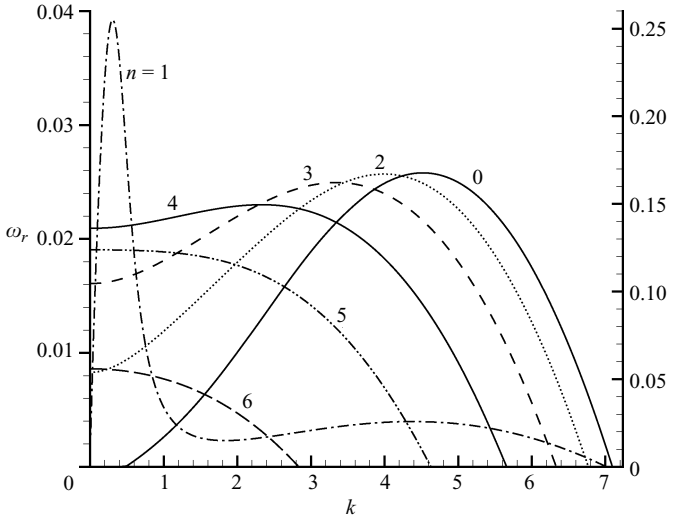

FIGURE 9. Comparison of the growth rates of the para-sinuous mode and the unstable non-axisymmetric modes. $\zeta = 0.75$, $Re = 1$.

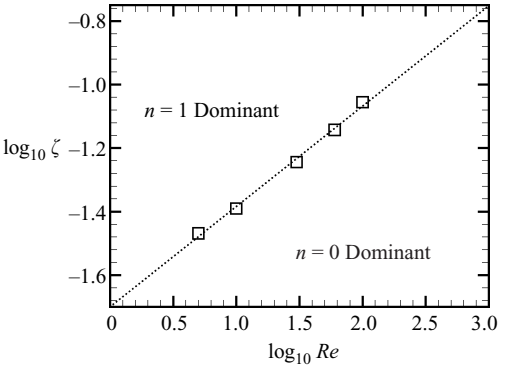

FIGURE 10. The boundary curve between the para-sinuous mode dominant region and helical mode dominant region in the (Re, ζ) plane.

Accordingly liquid viscosity may promote the predominance of the helical mode in the jet instability. That is, for highly viscous liquids the helical instability is easier to realize in experiments (Sun *et at*. 2003; Yu *et al*. 2004).

To investigate the effect of the electric field and liquid viscosity further, we compare the maximum growth rate of each mode, and obtain the boundary curve between the dominant regions of them in the (Re, ζ) plane. The curve is plotted in figure 10, where a log–log plot is represented for clarity. The square marks stand for data points, and the dotted line is the fitted boundary curve by means of the least-square method. The boundary curve is a straight line. The fitting shows that the relation between the critical electrical Euler number and critical Reynolds number is $\zeta = 0.020 Re^{0.32}$ approximately. Below the boundary curve is the dominant region of the para-sinuous mode, and above it is the dominant region of the helical mode. There is no dominant region for the other non-axisymmetric modes.

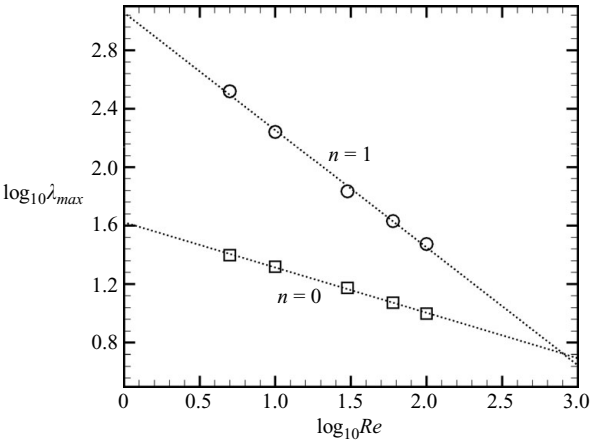

FIGURE 11. The most possible wavelengths of the para-sinuous mode and the helical mode on the boundary curve shown in figure 10.

In addition, the corresponding most possible wavelength $\lambda_{max} = 2\pi/k_{max}$ of the dominant modes is plotted in figure 11. The squares stand for data points of the para-sinuous mode, and the circles for the helical mode. The dotted lines are the fitted curve. The relation between the most possible wavelength and the critical Reynolds number is approximately linear in the log–log plot, $\lambda_{max} = 42.0Re^{-0.31}$ for the para-sinuous mode and $\lambda_{max} = 114.0Re^{-0.80}$ for the helical mode. As mentioned before, the most possible wavelength increases as the Reynolds number decreases.

3.3.2. *The low-Reynolds-number case*

It is well known that for a single liquid jet long waves are most unstable at low Reynolds numbers (Mestel 1996). The similar phenomenon is found in the coaxial jet case. As shown in figure 8(*b*), in the absence of electric field the maximum growth rate of the para-sinuous mode occurs near zero axial wavenumber. The result also shows that the helical mode is much more outstanding than the other unstable modes when liquid viscosity is high. The low-Reynolds-number case is of interest to research especially.

As $Re \ll 1$, the momentum equations (2.4) and (2.5) approximate to the Stokes equations, i.e.

$$\nabla p_1 = \frac{\mu_r}{Re}\nabla^2 \boldsymbol{u}_1, \quad \nabla p_2 = \frac{1}{Re}\nabla^2 \boldsymbol{u}_2. \tag{3.1}$$

Note that in the low-Reynolds-number case the density ratio $S = \rho_1/\rho_2$ and the basic velocity profile no more influence the jet instability. Imposing the normal mode decomposition on each physical quantity, we obtain the ordinary differential equations in the following component form:

$$\frac{\mathrm{d}\hat{u}_{mr}}{\mathrm{d}r} + \frac{\hat{u}_{mr}}{r} + \frac{\mathrm{i}n}{r}\hat{u}_{m\theta} + \mathrm{i}k\hat{u}_{mz} = 0,$$

$$\frac{\mathrm{d}^2\hat{u}_{mr}}{\mathrm{d}r^2} + \frac{1}{r}\frac{\mathrm{d}\hat{u}_{mr}}{\mathrm{d}r} - \left(k^2 + \frac{n^2+1}{r^2}\right)\hat{u}_{mr} - \frac{2\mathrm{i}n}{r^2}\hat{u}_{m\theta} = \frac{Re}{\delta_{m2} + \mu_r\delta_{m1}}\frac{\mathrm{d}\hat{p}_m}{\mathrm{d}r},$$

$$\frac{\mathrm{d}^2\hat{u}_{m\theta}}{\mathrm{d}r^2} + \frac{1}{r}\frac{\mathrm{d}\hat{u}_{m\theta}}{\mathrm{d}r} - \left(k^2 + \frac{n^2+1}{r^2}\right)\hat{u}_{m\theta} + \frac{2\mathrm{i}n}{r^2}\hat{u}_{mr} = \frac{Re}{\delta_{m2} + \mu_r\delta_{m1}}\frac{\mathrm{i}n\hat{p}_m}{r},$$

$$\frac{\mathrm{d}^2\hat{u}_{mz}}{\mathrm{d}r^2}+\frac{1}{r}\frac{\mathrm{d}\hat{u}_{mz}}{\mathrm{d}r}-\left(k^2+\frac{n^2}{r^2}\right)\hat{u}_{mz}=\frac{Re}{\delta_{m2}+\mu_r\delta_{m1}}\mathrm{i}k\hat{p}_m,$$

where the subscript $m=1, 2$ stands for the inner and outer liquids, respectively, δ is the Kronecker function. The solutions are

$$\begin{aligned}
\hat{p}_1(r) &= A_1 I_n(kr),\\
\hat{u}_{1r}(r) &= A_2 I_{n-1}(kr)+A_3 I_{n+1}(kr)+\frac{Rer}{2\mu_r}A_1 I_n(kr)-\frac{Re(n+2)}{2k\mu_r}A_1 I_{n+1}(kr),\\
\hat{u}_{1\theta}(r) &= \mathrm{i}A_2 I_{n-1}(kr)-\mathrm{i}A_3 I_{n+1}(kr)+\frac{\mathrm{i}Re(n+2)}{2k\mu_r}A_1 I_{n+1}(kr),\\
\hat{u}_{1z}(r) &= \mathrm{i}\,(A_2+A_3)\,I_n(kr)+\frac{\mathrm{i}Rer}{2\mu_r}A_1 I_{n+1}(kr),\\
\hat{p}_2(r) &= A_4 I_n(kr)+A_5 K_n(kr),\\
\hat{u}_{2r}(r) &= A_6 I_{n-1}(kr)+A_7 I_{n+1}(kr)+A_8 K_{n-1}(kr)+A_9 K_{n+1}(kr)\\
&\quad+\frac{Rer}{2}\left[A_4 I_n(kr)+A_5 K_n(kr)\right]-\frac{Re(n+2)}{2k}\left[A_4 I_{n+1}(kr)-A_5 K_{n+1}(kr)\right],\\
\hat{u}_{2\theta}(r) &= \mathrm{i}A_6 I_{n-1}(kr)-\mathrm{i}A_7 I_{n+1}(kr)+\mathrm{i}A_8 K_{n-1}(kr)-\mathrm{i}A_9 K_{n+1}(kr)\\
&\quad+\frac{\mathrm{i}Re(n+2)}{2k}\left[A_4 I_{n+1}(kr)-A_5 K_{n+1}(kr)\right],\\
\hat{u}_{2z}(r) &= \mathrm{i}\,(A_6+A_7)\,I_n(kr)-\mathrm{i}\,(A_8+A_9)\,K_n(kr)+\frac{\mathrm{i}Rer}{2}\left[A_4 I_{n+1}(kr)-A_5 K_{n+1}(kr)\right],
\end{aligned}$$

where A_1–A_9 are coefficients to be determined. Substituting the solutions into the boundary conditions, we obtain a homogeneous linear system comprising 12 equations. There are correspondingly 12 unknown quantities, i.e. A_1–A_9, $\hat{\eta}_1$, $\hat{\eta}_2$ and $\hat{q}_s$. The system has non-trivial solution only if the determinant of its coefficient matrix is null, which gives the dispersion relation. The dispersion relation in the low-Reynolds-number case is a cubic equation of the complex growth rate ω, i.e.

$$\omega^3+a_1\omega^2+a_2\omega+a_3=0. \tag{3.2}$$

Furthermore, supposing $k\to 0$, we obtain the dispersion relation in the long wavelength limit, which has the same form as (3.2). The expressions of coefficients a_1, a_2 and a_3 are too long to represent here. The dispersion relation can be solved numerically. There are three solutions. Each corresponds to one mode. Two are usually unstable for axisymmetric instability, corresponding to the para-varicose mode and para-sinuous mode, respectively. One is unstable for non-axisymmetric instability.

Figures 12(*a*) and 12(*b*) illustrate the para-sinuous mode and helical mode, respectively, in the low-Reynolds-number case, where $Re=0.1$. Because the electric field is relatively small, the non-axisymmetric modes $n>1$ are stable. In figure 12(*a*) the most possible wavenumber k_{max} of the para-sinuous mode is zero when the electrical Euler number $\zeta=0$. As the electric field increases, k_{max} moves away from zero to long wavelength region. In figure 12(*b*) the helical mode is unstable in long wavelength region. The growth rate of it is three orders of magnitude larger than that of the para-sinuous mode, and therefore the helical instability is definitely dominant in the breakup process of the jet. Furthermore, in the low-Reynolds-number case, the helical mode predominates over the others even when the radial electric field is considerably small. According to the fitting in figure 10, it is concluded that the critical electrical Euler number is 0.020 as $Re\to 0$.

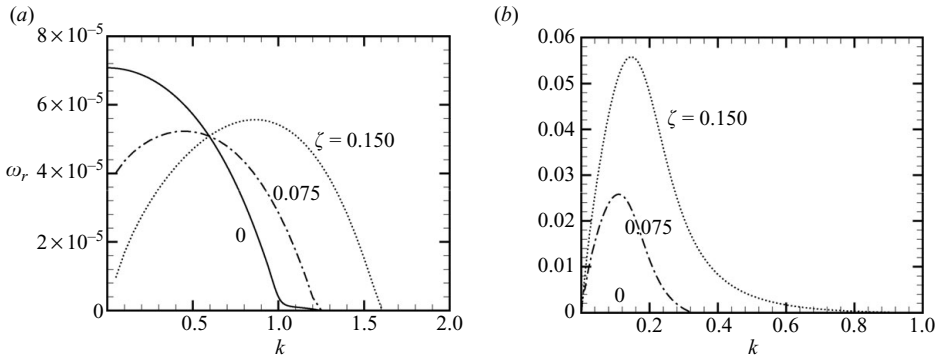

FIGURE 12. The effect of the radial electric field on the growth rates of (*a*) the para-sinuous mode $n=0$ and (*b*) the helical mode $n=1$. $Re=0.1$.

3.3.3. *Energy budget*

In the above analysis one question is why liquid viscosity dampens the axisymmetric instability much more than the helical instability. To better understand the mechanism in it, we carry out an energy budget. Because of the complexity of the present model, we propose a simple theoretical model to evaluate the energy parts involved in the perturbed state.

Consider a single liquid jet of uniform basic velocity U, subjected to a radial electric field of magnitude $-V_0/[r\ln(R/R_0)]$, where R is the radius of the jet and R_0 is the radius of the annular electrode. The liquid is a perfect conductor of infinite electrical conductivity. The density and viscosity of it is denoted by ρ and μ, respectively. The surface tension on the jet surface is γ. The hydrodynamic effect of the air surrounding the jet is neglected.

Suppose the jet is perturbed by an infinitesimal three-dimensional disturbance at initial time. A temporal linear instability in terms of the normal mode method gives the dispersion relation of the following dimensionless form (Avital 1995; Li *et al.* 2007):

$$\begin{vmatrix} 2\mathrm{i}kI_n'(k) & -I_{n+1}(l)-\dfrac{l^2}{k^2}I_n'(l) & I_{n-1}(l)+\dfrac{l^2}{k^2}I_n'(l) \\ 2\mathrm{i}nk\left(I_n'(k)-\dfrac{I_n(k)}{k}\right) & lI_{n+2}(l) & lI_{n-2}(l) \\ D_1 & D_2 & D_3 \end{vmatrix} = 0, \tag{3.3}$$

where

$$\begin{aligned} l &= \sqrt{k^2+Re(\omega+\mathrm{i}k)}, \\ D_1 &= (\omega+\mathrm{i}k)I_n(k)+\frac{2k^2}{Re}I_n''(k)+\frac{kTI_n'(k)}{\omega+\mathrm{i}k}, \\ D_2 &= \frac{2\mathrm{i}l}{Re}I_{n+1}'(l)+\frac{\mathrm{i}TI_{n+1}(l)}{\omega+\mathrm{i}k}, \\ D_3 &= -\frac{2\mathrm{i}l}{Re}I_{n-1}'(l)-\frac{\mathrm{i}TI_{n-1}(l)}{\omega+\mathrm{i}k}, \\ T &= \zeta\left(1+k\frac{K_n'(k)}{K_n(k)}\right)-\frac{1}{We}(1-n^2-k^2). \end{aligned}$$

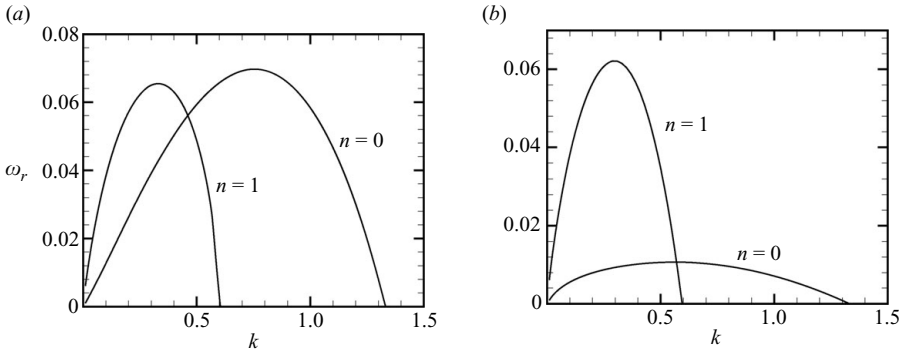

FIGURE 13. Comparison of the varicose mode and the kink mode for a single liquid jet under a radial electric field. (*a*) $Re = 10$ and (*b*) $Re = 1$. $We = 10$, $\zeta = 0.1$.

The symbol $''$ denotes the second derivative of the corresponding Bessel function with respect to the argument. The relevant dimensionless parameters are the Reynolds number $Re = \rho U R/\mu$, the Weber number $We = \rho U^2 R/\gamma$ and the electrical Euler number $\zeta = \varepsilon_3 V_0^2/\rho U^2 R^2 \ln^2(R/R_0)$.

The dispersion relation (3.3) can be solved numerically. The unstable mode for the axisymmetric instability $n = 0$ is usually called varicose mode, and the mode for the non-axisymmetric instability $n = 1$ is called kink mode (Son & Ohba 1998). Figure 13 illustrates the growths rates of the varicose mode and the kink mode at different Reynolds numbers. In the calculation the electrical Euler number is kept at a small number ($\zeta = 0.1$) so that the non-axisymmetric instability $n > 1$ are stable. At a relatively large Reynolds number $Re = 10$ as shown in figure 13(*a*), the kink mode is comparable to the varicose mode. In such a case both are possibly dominant in the jet breakup. However, at a relatively small Reynolds number $Re = 1$ as shown in figure 13(*b*), the growth rate of the kink mode is much larger than that of the varicose mode. In such a case the kink mode is obviously dominant. The result indicates that higher viscosity favours the predominance of the kink mode and helps the realization of electrospinning in experiments.

The method of energy budget can be referred to Lin (2003). The main procedure is as follows. Calculating the dot product of the momentum equation of disturbance with the velocity perturbation $\boldsymbol{u}$, integrating the equation over a control volume of one wavelength $\lambda = 2\pi/k$ and one period $T = 2\pi/\omega_i$ (ω_i is the imaginary part of the complex growth rate ω), using the continuity equation and Gauss theorem to transform volume integrals into surface integrals, and averaging the integrals over λ and T, we obtain the energy equation

$$\frac{1}{T\lambda}\int_0^T \iiint_V \left(\frac{\partial}{\partial t} + \frac{\partial}{\partial z}\right) e \mathrm{d}V \mathrm{d}t = -\frac{1}{T\lambda}\int_0^T \oiint_A p\boldsymbol{u}\cdot\boldsymbol{n}\mathrm{d}A\mathrm{d}t + \frac{1}{T\lambda Re}\int_0^T \oiint_A (\boldsymbol{u}\cdot\boldsymbol{\tau})\cdot\boldsymbol{n}\mathrm{d}A\mathrm{d}t - \frac{1}{2ReT\lambda}\int_0^T \iiint_V \boldsymbol{\tau}\cdot\boldsymbol{\tau}\mathrm{d}V\mathrm{d}t, \tag{3.4}$$

where $e = \boldsymbol{u}\cdot\boldsymbol{u}/2$ is the kinetic energy of disturbance, V and A are the control volume and corresponding surface, respectively, and $\boldsymbol{\tau} = \nabla\boldsymbol{u} + (\nabla\boldsymbol{u})^{\mathrm{T}}$ is the strain rate tensor where the superscript T means transposition. The left-hand side of (3.4) represents the change rate of the disturbance kinetic energy. Three terms on the right-hand side represent the work done by pressure, the work done by viscous stress and the

energy dissipation through viscosity. Applying the kinematic and dynamic boundary conditions to (3.4), it yields

$$KE = PRL + SUT + ELF + SHL + NVL + DIS, \tag{3.5}$$

where

$$KE = \frac{1}{T\lambda}\int_0^T\int_0^\lambda\int_0^{2\pi}\int_0^1 \frac{1}{2}\left(\frac{\partial}{\partial t}+\frac{\partial}{\partial t}\right)\left(u_r^2+u_\theta^2+u_z^2\right) r\,\mathrm{d}r\,\mathrm{d}\theta\,\mathrm{d}z\,\mathrm{d}t,$$

$$PRL = -\frac{1}{T\lambda}\int_0^T\int_0^{2\pi}\int_0^1 [pu_z]_{z=0}^{z=\lambda} r\,\mathrm{d}r\,\mathrm{d}\theta\,\mathrm{d}t,$$

$$SUT = \frac{1}{T\lambda We}\int_0^T\int_0^\lambda\int_0^{2\pi} [u_r\hat{\eta}(1-n^2-k^2)]_{r=1}\,\mathrm{d}\theta\,\mathrm{d}z\,\mathrm{d}t,$$

$$ELF = -\frac{\zeta}{T\lambda}\int_0^T\int_0^\lambda\int_0^{2\pi}\left[u_r\hat{\eta}\left(1+k\frac{K_n'(k)}{K_n(k)}\right)\right]_{r=1}\mathrm{d}\theta\,\mathrm{d}z\,\mathrm{d}t,$$

$$SHL = \frac{1}{T\lambda Re}\int_0^T\int_0^{2\pi}\int_0^1\left[u_r\left(\frac{\partial u_r}{\partial z}+\frac{\partial u_z}{\partial r}\right)+u_\theta\left(\frac{\partial u_\theta}{\partial z}+\frac{\partial u_z}{r\partial\theta}\right)\right]_{z=0}^{z=\lambda} r\,\mathrm{d}r\,\mathrm{d}\theta\,\mathrm{d}t,$$

$$NVL = \frac{1}{T\lambda Re}\int_0^T\int_0^{2\pi}\int_0^1\left[2u_z\frac{\partial u_z}{\partial z}\right]_{z=0}^{z=\lambda} r\,\mathrm{d}r\,\mathrm{d}\theta\,\mathrm{d}t,$$

$$DIS = -\frac{1}{T\lambda Re}\int_0^T\int_0^\lambda\int_0^{2\pi}\int_0^1\left[2\left(\frac{\partial u_r}{\partial r}\right)^2+2\left(\frac{\partial u_\theta}{r\partial\theta}+\frac{u_r}{r}\right)^2+2\left(\frac{\partial u_z}{\partial z}\right)^2\right.$$
$$\left.+\left(\frac{\partial u_r}{r\partial\theta}+\frac{\partial u_\theta}{\partial r}-\frac{u_\theta}{r}\right)^2+\left(\frac{\partial u_r}{\partial z}+\frac{\partial u_z}{\partial r}\right)^2+\left(\frac{\partial u_\theta}{\partial z}+\frac{\partial u_z}{r\partial\theta}\right)^2\right] r\,\mathrm{d}r\,\mathrm{d}\theta\,\mathrm{d}z\,\mathrm{d}t.$$

KE on the left-hand side of (3.5) represents the change rate of the disturbance kinetic energy. There are six terms on the right-hand side. Each of them represents a physical mechanism affecting the jet instability. PRL is the rate of work done by the pressure at the two ends of the control volume, SUT and ELF are the rates of work done by the surface tension and radial electric field at the jet surface, respectively, SHL and NVL are the rates of work done by the tangential and normal viscous stresses at the two ends of the control volume, respectively, and DIS is the rate of energy dissipation through liquid viscosity in volume. Obviously, DIS is always negative. The integrals are calculated by using the IMSL subroutine QAND. Each of the integrals is calculated independently. Hence the comparison between the sum of all the terms on the right-hand side and KE on the left-hand side provides a simple check for the calculation accuracy.

Figure 14 illustrates the energy budget for the single liquid jet under the radial electric field at two typical values of the Reynolds number. All the energy terms are normalized with the value of KE corresponding to the most possible wave-number of the varicose mode at the same Reynolds number. The terms PRL, SHL and NVL are usually five to eight orders of magnitude smaller than KE. Therefore they are negligible in energy budget. From figures 14(a) and 14(c) it can be seen that the varicose mode in the Rayleigh regime belongs to capillary instability caused by surface tension (Shen & Li 1996). The work done by surface tension is positive at the axial wavenumber $k < 1$. From a physical point of view, surface tension tends to make the area per unit mass smaller and drives towards the formation of droplets in the jet breakup process. However, viscosity tries to decelerate the change in shape

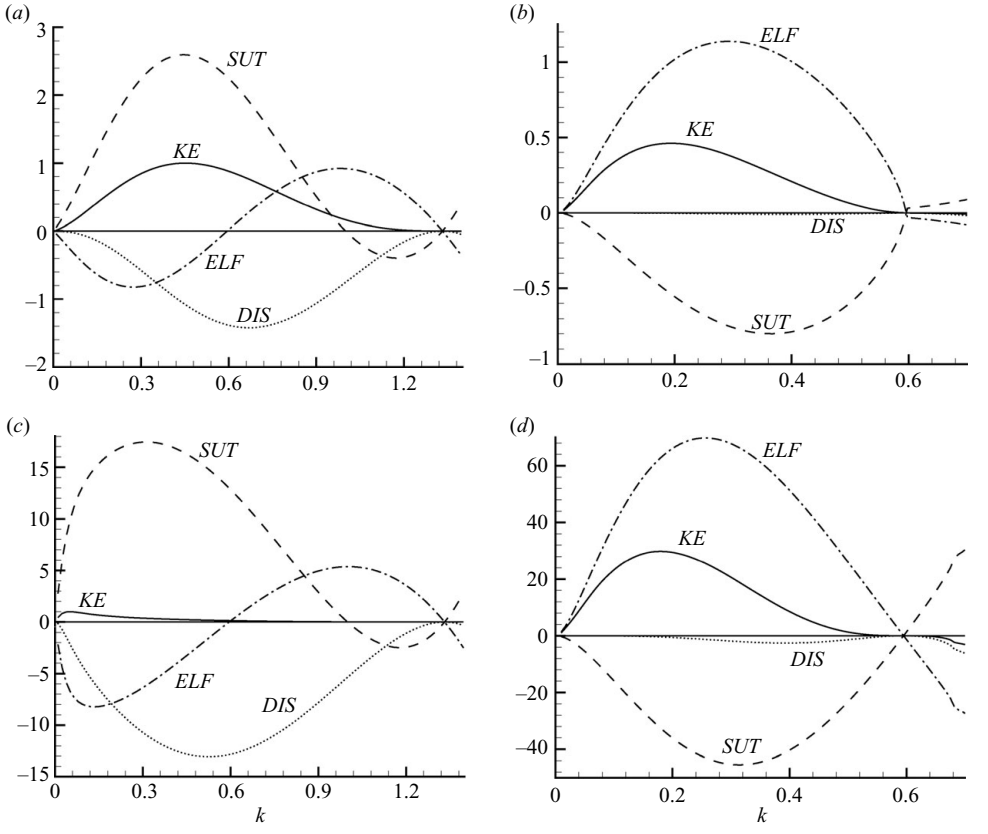

FIGURE 14. Energy budget for a single liquid jet under a radial electric field. (*a*) The varicose mode, $n=0$, $Re=10$, (*b*) the kink mode, $n=1$, $Re=10$, (*c*) the varicose mode, $n=0$, $Re=1$ and (*d*) the kink mode, $n=1$, $Re=1$. KE: the disturbance kinetic energy; SUT: the work done by the surface tension; ELF: the work done by the radial electric field; DIS: the mechanical energy dissipation through the viscosity of liquid. $We=10$, $\zeta=0.1$.

through viscous dissipation. In such a way the varicose mode is suppressed. On the other hand, the work done by the electric field is negative in the long wavelength region $k<0.6$, which weakens the destabilizing effect of surface tension. For the kink mode, as shown in figures 14(*b*) and 14(*d*), only the electric field does positive work in long wavelength region. The work done by surface tension is negative. DIS corresponding to viscous dissipation is small compared to ELF and SUT, and also much smaller than DIS for the varicose mode. Therefore, on the one hand, liquid viscosity suppresses the varicose instability of the jet more than the kink instability, while on the other hand, radial electric field promotes the kink instability more than the varicose instability. In the single-liquid electrospinning experiments (Fong, Chun & Reneker 1999; Zuo *et al.* 2005), it was found that the kink instability is easier to be predominant for higher liquid viscosity and higher electric field. Our analysis accords well with the experimental result.

3.4. *Effect of the interface tensions on the jet instability*

In the theoretical model there are two dimensionless numbers related to interface tension. They are the Weber number $We=\rho_2U^2R_2/\gamma_2$ and the interface tension coefficient ratio $\Gamma=\gamma_1/\gamma_2$. The Weber number We represents the magnitude of

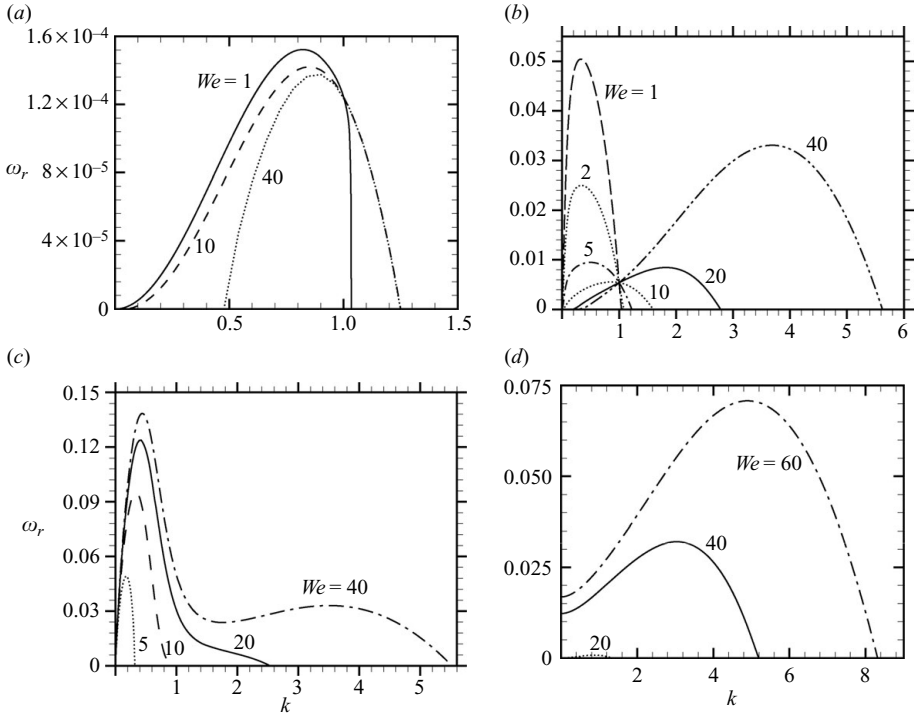

FIGURE 15. The effect of the interface tension of the outer interface on the growth rates of (*a*) the para-varicose mode $n=0$, (*b*) the para-sinuous mode $n=0$, (*c*) the helical mode $n=1$ and (*d*) the non-axisymmetric mode $n=2$. $We_1=43.5$.

surface tension on the outer interface relative to the inertial force. The surface tension on the inner interface can be represented by a combined dimensionless parameter $We_1=We/\Gamma$. In the reference state $We_1=43.5$. We and We_1 may have different effect on the jet instability. They are investigated individually.

3.4.1. *Effect of the interface tension of the outer interface*

Figures 15(*a*)–15(*d*) illustrate the effect of the interface tension of the outer interface on the para-varicose mode, para-sinuous mode, helical mode and non-axisymmetric mode $n=2$, respectively, where We_1 is fixed to the value in the reference state. Like the radial electric field, the interface tension at the outer interface has a two-fold effect on the para-varicose mode and para-sinuous mode: in long wavelength region where the axial wavenumber is smaller than a critical value ($k<k_{crit}$, $k_{crit}\approx 1$) the growth rates of the modes are reduced as We increases, while in relatively short wavelength region where $k>k_{crit}$ the growth rates are increased. The effect of We on the para-sinuous mode is more profound than on the para-varicose mode. For long waves $k<k_{crit}$ the interface tension at the outer interface does positive work, and therefore the disturbance kinetic energy is increased; conversely, for relatively short waves $k>k_{crit}$ the work is negative, and the kinetic energy is reduced. The growth rate of the helical mode is always increased as the Weber number increases, as shown in figure 15(*c*). Similarly, in figure 15(*d*) the non-axisymmetric mode $n=2$ becomes unstable only if the Weber number is sufficiently large. For the helical mode and the non-axisymmetric modes with azimuthal wavenumber $n>1$ the work done by the

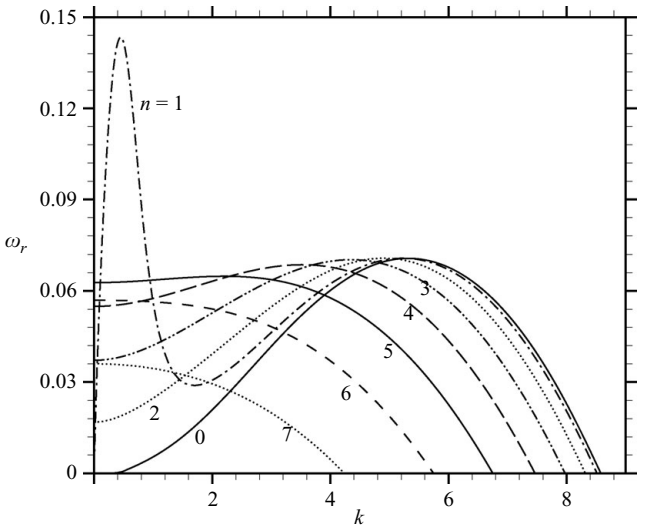

FIGURE 16. Comparison of the growth rates of the para-sinuous mode and the unstable non-axisymmetric modes. $We = 60$, $We_1 = 43.5$.

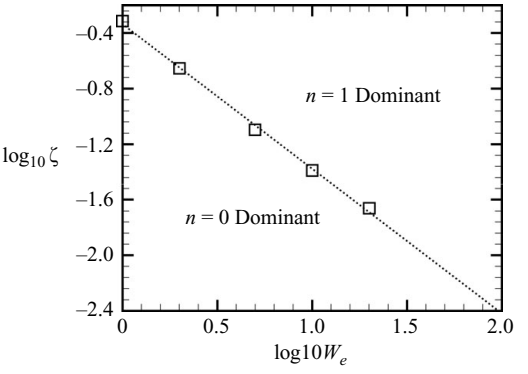

FIGURE 17. The boundary curve between the para-sinuous mode dominant region and helical mode dominant region in the (We, ζ) plane. $We_1 = 43.5$.

interface tension at the outer interface is negative. The non-axisymmetric instability is suppressed as the interface tension increases.

At relatively large Weber numbers the non-axisymmetric modes having higher azimuthal wavenumber also become unstable. Figure 16 illustrates the comparison of them with the para-sinuous and the helical mode where the Weber number is fixed to 60. The phenomenon seems similar to that in relatively high radial electric field. In the figure the non-axisymmetric modes up to $n = 7$ are unstable. The non-axisymmetric modes $n > 1$ are most unstable at zero wavenumber. The helical mode dominates in long wavelength region. In short wavelength region the para-sinuous mode, helical mode and non-axisymmetric modes $n > 1$ have growth rates close to each other. In this region it is hard to say which mode is dominant.

Comparing the maximum growth rate of each mode, we plot the boundary curve between the dominant regions in the (We, ζ) plane. A log–log plot is shown in figure 17, where the squares stand for data points, and the dotted line is the fitted

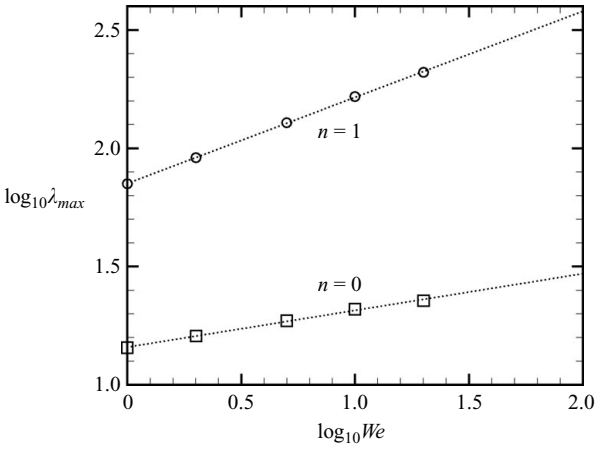

FIGURE 18. The most possible wavelengths of the para-sinuous mode and the helical mode on the boundary curve shown in figure 17. $We_1 = 43.5$.

boundary curve. Below the line is the dominant region of the para-sinuous mode, and above it is the dominant region of the helical mode. There is no dominant region of the other non-axisymmetric modes in the value range investigated. It is clear that at large Weber numbers the helical instability becomes predominant even when the electric field is considerably small. The boundary is a straight line in the log–log plot. The fitting shows the relation between the critical electrical Euler number and critical Weber number is $\zeta = 0.46We^{-1.0}$ approximately. The corresponding most possible wavelength λ_{max} on the boundary curve is plotted in figure 18. As the Weber number increases, the most possible wavelength increases for both the modes. The relation between λ_{max} and the critical Weber number is approximately linear in the log–log plot. The fitting yields the relation $\lambda_{max} = 14.4We^{-0.155}$ for the para-sinuous mode and $\lambda_{max} = 71.0We^{-0.36}$ for the helical mode.

3.4.2. *Effect of the interface tension of the inner interface*

The effect of the interface tension of the inner interface on the growth rates of the para-varicose mode, para-sinuous mode and helical mode is shown in figures 19(*a*)–19(*c*), respectively. It can be seen in the figure that the interface tension on the inner interface has a remarkable destabilizing effect on the para-varicose mode and para-sinuous mode in the Rayleigh regime. Compared with the interface tension on the outer interface, its stabilization effect on the modes in relatively short wavelength region is not very evident. On the other hand, the interface tension on the inner interface suppresses the helical instability significantly. The non-axisymmetric modes with azimuthal wavenumber $n > 1$ are stable within the value range investigated.

3.5. *Effect of the radius ratio on the jet instability*

The radius ratio of the inner to outer liquid of the jet $a = R_1/R_2$ is the only geometric parameter involved in this problem. Its effect on the para-varicose mode, para-sinuous mode, helical mode and non-axisymmetric mode $n = 2$ is shown in figures 20(*a*)–20(*d*), respectively, where the electrical Euler number is fixed to 0.45. It can be seen in the figure that the growth rates of all the modes are diminished as the radius ratio a increases. Relatively, the maximum growth rate of the helical mode is reduced less than the others, indicating that a thinner gap between the inner and outer interfaces of the jet favours the predominance of the helical instability. The corresponding most

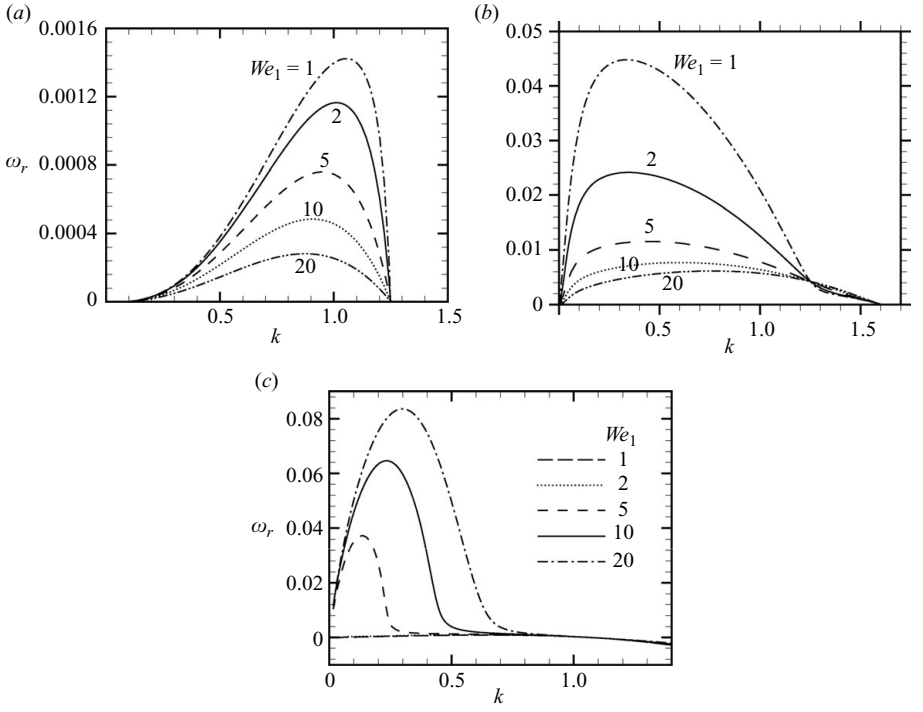

FIGURE 19. The effect of the interface tension of the inner interface on the growth rates of (*a*) the para-varicose mode $n = 0$, (*b*) the para-sinuous mode $n = 0$ and (*c*) the helical mode $n = 1$.

possible wavelength moves towards long wavelength region as a increases. The result also shows that the radius ratio has no influence on the cut-off wavenumbers of the unstable modes except the para-varicose one.

4. Conclusions

The temporal linear instability of a viscous coaxial jet in a radial electric field is studied. Both the axisymmetric and non-axisymmetric instability are investigated. The radial electric field is found to induce the instability of the non-axisymmetric modes. In the absence of electric field, the non-axisymmetric modes are all stable and the para-sinuous mode is dominant. At sufficiently large electric field, the non-axisymmetric modes become unstable. For non-axisymmetric instability of a certain azimuthal wavenumber, there is usually one unstable mode. The smaller the azimuthal wavenumber, the easier the non-axisymmetric mode to destabilize. The radial electric field has a strong destabilizing effect on the non-axisymmetric modes, especially on the helical one. The helical mode is the most unstable at sufficiently large electric field. Moreover, the most possible wavenumbers of all the modes become large as the electric field increases. Non-axisymmetric modes with azimuthal wavenumber $n > 1$ may be the most unstable at zero axial wavenumber. The influence of the electrical permittivities of the inner and outer liquids as well as the electrical relaxation time of the driving liquid on the jet instability is limited. Liquid viscosity stabilizes all modes, especially the para-sinuous and non-axisymmetric modes $n > 1$. The helical mode is dominant when liquid viscosity is high. The interface tensions of the inner and outer interfaces have a great effect on the jet instability. The para-sinuous mode

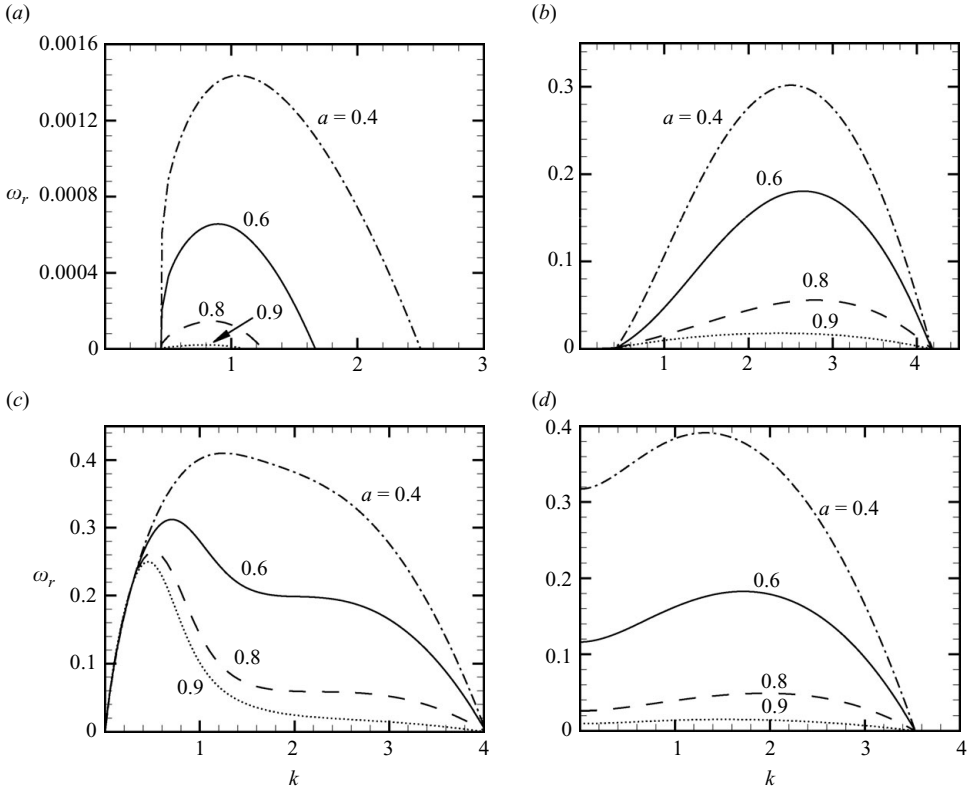

FIGURE 20. The effect of the radius ratio of the inner to outer liquids on the growth rates of (*a*) the para-varicose mode $n=0$, (*b*) the para-sinuous mode $n=0$, (*c*) the helical mode $n=1$ and (*d*) the non-axisymmetric mode $n=2$. $\zeta=0.45$.

is destabilized by interface tension in long wavelength region. Conversely, the helical mode and the non-axisymmetric modes $n>1$ are stabilized by interface tension. All the unstable modes are found to be depressed as the gap between the inner and outer interfaces of the jet becomes narrow. In general, relatively small radial electric field, low liquid viscosity and high interface tension favour the predominance of the para-sinuous mode and the realization of coaxial electrospraying in experiments; conversely, relatively large radial electric field, high liquid viscosity and low interface tension help the helical mode dominate in the jet instability, and hence coaxial electrospinning is most likely to be realized in experiments.

The authors are indebted to the referees for their valuable comments that helped to improve the manuscript. The work was supported by the National Natural Science Foundation of China (Project No. 10802084, 10572137).

Appendix: Equations

The equations can be written in a condensed form as follows:

$$\boldsymbol{A}\boldsymbol{F}=\omega\boldsymbol{B}\boldsymbol{F},$$

where $\boldsymbol{F}$ is a vector comprising all the eigenfunctions, i.e.

$$\boldsymbol{F}=(\hat{u}_{1r}(r),\hat{u}_{1\theta}(r),\hat{u}_{1z}(r),\hat{p}_1(r),\hat{u}_{2r}(r),\hat{u}_{2\theta}(r),\hat{u}_{2z}(r),\hat{p}_2(r),\hat{q}_s,\hat{\eta}_1,\hat{\eta}_2)^{\mathrm{T}}.$$

The eigenfunctions $\hat{u}_{1r}$, $\hat{u}_{1\theta}$, $\hat{u}_{1z}$ and $\hat{p}_1$ are related to the inner liquid; $\hat{u}_{2r}$, $\hat{u}_{2\theta}$, $\hat{u}_{2z}$ and $\hat{p}_2$ are related to the outer liquid. They are the functions of variable r. $\hat{\eta}_1$ is related to the inner interface; $\hat{\eta}_2$ and $\hat{q}_s$ are related to the outer interface. They are constants.

The expressions of the matrices $\boldsymbol{A}$ and $\boldsymbol{B}$ are

$$\boldsymbol{A}=\begin{pmatrix}
\frac{\mu_r D^{\dagger\dagger}}{SRe} & -\frac{2in\mu_r}{r^2SRe} & 0 & -\frac{D}{S} & 0 & 0 & 0 & 0 & 0 & 0 & 0\\
\frac{2n\mu_r}{r^2SRe} & \frac{\mu_r D^{\dagger\dagger}}{SRe} & 0 & -\frac{in}{Sr} & 0 & 0 & 0 & 0 & 0 & 0 & 0\\
0 & 0 & \frac{\mu_r D^{\dagger}}{SRe} & -\frac{ik}{S} & 0 & 0 & 0 & 0 & 0 & 0 & 0\\
D^* & \frac{in}{r} & ik & 0 & 0 & 0 & 0 & 0 & 0 & 0 & 0\\
0 & 0 & 0 & 0 & \frac{D^{\dagger\dagger}}{Re} & -\frac{2in}{r^2Re} & 0 & -D & 0 & 0 & 0\\
0 & 0 & 0 & 0 & \frac{2in}{r^2Re} & \frac{D^{\dagger\dagger}}{Re} & 0 & -\frac{in}{r} & 0 & 0 & 0\\
0 & 0 & 0 & 0 & 0 & 0 & \frac{D^{\dagger}}{Re} & -ik & 0 & 0 & 0\\
0 & 0 & 0 & 0 & D^* & \frac{in}{r} & ik & 0 & 0 & 0 & 0\\
0 & 0 & 0 & 0 & D & 0 & 0 & 0 & G_1 & 0 & G_2\\
1 & 0 & 0 & 0 & 0 & 0 & 0 & 0 & 0 & 0 & 0\\
0 & 0 & 0 & 0 & 1 & 0 & 0 & 0 & 0 & 0 & 0
\end{pmatrix}$$

and

$$\boldsymbol{B}=\begin{pmatrix}
1 & 0 & 0 & 0 & 0 & 0 & 0 & 0 & 0 & 0 & 0\\
0 & 1 & 0 & 0 & 0 & 0 & 0 & 0 & 0 & 0 & 0\\
0 & 0 & 1 & 0 & 0 & 0 & 0 & 0 & 0 & 0 & 0\\
0 & 0 & 0 & 0 & 0 & 0 & 0 & 0 & 0 & 0 & 0\\
0 & 0 & 0 & 0 & 1 & 0 & 0 & 0 & 0 & 0 & 0\\
0 & 0 & 0 & 0 & 0 & 1 & 0 & 0 & 0 & 0 & 0\\
0 & 0 & 0 & 0 & 0 & 0 & 1 & 0 & 0 & 0 & 0\\
0 & 0 & 0 & 0 & 0 & 0 & 0 & 0 & 0 & 0 & 0\\
0 & 0 & 0 & 0 & 0 & 0 & 0 & 0 & 1 & 0 & 0\\
0 & 0 & 0 & 0 & 0 & 0 & 0 & 0 & 0 & 1 & 0\\
0 & 0 & 0 & 0 & 0 & 0 & 0 & 0 & 0 & 0 & 1
\end{pmatrix},$$

respectively, where

$$D=\frac{\mathrm{d}}{\mathrm{d}r},\quad D^*=\frac{\mathrm{d}}{\mathrm{d}r}+\frac{1}{r},\quad D^{\dagger}=\frac{\mathrm{d}^2}{\mathrm{d}r^2}+\frac{1}{r}\frac{\mathrm{d}}{\mathrm{d}r}-k^2-\frac{n^2}{r^2},\quad D^{\dagger\dagger}=D^{\dagger}-\frac{1}{r^2},$$

$$G_1=-\frac{\tau\varepsilon_{r2}D_1}{D_2\xi+D_1\varepsilon_{r2}},\quad G_2=-\frac{\tau\varepsilon_{r2}D_1(1+k\xi)}{D_2\xi+D_1\varepsilon_{r2}},\quad \xi=\frac{K'_n(k)}{K_n(k)},$$

$$D_1=-K'_n(k)\left(1-\frac{\varepsilon_{r2}}{\varepsilon_{r1}}\right)+I'_n(k)\left(\frac{K_n(ka)}{I_n(ka)}-\frac{\varepsilon_{r2}}{\varepsilon_{r1}}\frac{K'_n(ka)}{I'_n(ka)}\right),$$

$$D_2=K_n(k)\left(1-\frac{\varepsilon_{r2}}{\varepsilon_{r1}}\right)-I_n(k)\left(\frac{K_n(ka)}{I_n(ka)}-\frac{\varepsilon_{r2}}{\varepsilon_{r1}}\frac{K'_n(ka)}{I'_n(ka)}\right).$$

$I_n(x)$and $K_n(x)$ are the nth-order modified Bessel functions of the first and second kinds, respectively. The prime denotes the derivative of the corresponding Bessel function with respect to the argument x.

The boundary conditions are as follows:

at $r = 0$,

$$\hat{u}_{1r} = \hat{u}_{1\theta} = \frac{\mathrm{d}\hat{u}_{1z}}{\mathrm{d}r} = \frac{\mathrm{d}\hat{p}_1}{\mathrm{d}r} = 0 \quad \text{for} \quad n = 0,$$

$$\hat{u}_{1z} = \hat{p}_1 = 0, \quad \hat{u}_{1r} + \mathrm{i}\hat{u}_{1\theta} = 0, \quad 2\frac{\mathrm{d}\hat{u}_{1r}}{\mathrm{d}r} + \mathrm{i}\frac{\mathrm{d}\hat{u}_{1\theta}}{\mathrm{d}r} = 0 \quad \text{for} \quad n = 1,$$

$$\hat{u}_{1r} = \hat{u}_{1\theta} = \hat{u}_{1z} = \hat{p}_1 = 0 \quad \text{for} \quad n > 1;$$

at $r = a + \eta_1$,

$$\hat{u}_{1r} = \hat{u}_{2r}, \quad \hat{u}_{1\theta} = \hat{u}_{2\theta}, \quad \hat{u}_{1z} = \hat{u}_{2z},$$

$$\mathrm{i}k\hat{u}_{2r} + \frac{\mathrm{d}\hat{u}_{2z}}{\mathrm{d}r} - \mu_r\left(\mathrm{i}k\hat{u}_{1r} + \frac{\mathrm{d}\hat{u}_{1z}}{\mathrm{d}r}\right) = 0,$$

$$\frac{\mathrm{i}n}{a}\hat{u}_{2r} + \frac{\mathrm{d}\hat{u}_{2\theta}}{\mathrm{d}r} - \frac{\hat{u}_{2\theta}}{a} - \mu_r\left(\frac{\mathrm{i}n}{a}\hat{u}_{1r} + \frac{\mathrm{d}\hat{u}_{1\theta}}{\mathrm{d}r} - \frac{\hat{u}_{1\theta}}{a}\right) = 0,$$

$$\hat{p}_1 - \frac{2\mu_r}{Re}\frac{\mathrm{d}\hat{u}_{1r}}{\mathrm{d}r} - \hat{p}_2 + \frac{2}{Re}\frac{\mathrm{d}\hat{u}_{2r}}{\mathrm{d}r} + \frac{\Gamma}{Wea^2}[1 - n^2 - (ka)^2]\hat{\eta}_1 = 0;$$

at $r = 1 + \eta_2$,

$$\mathrm{i}k\hat{u}_{2r} + \frac{\mathrm{d}\hat{u}_{2z}}{\mathrm{d}r} - \hat{q}_s\frac{\mathrm{i}\zeta ReD_2}{D_2\xi + D_1\varepsilon_{r2}} - \hat{\eta}_2\frac{\mathrm{i}\zeta ReD_2(1 + k\xi)}{D_2\xi + D_1\varepsilon_{r2}} = 0,$$

$$n\frac{\mathrm{d}\hat{u}_{2z}}{\mathrm{d}r} - k\left(\frac{\mathrm{d}\hat{u}_{2\theta}}{\mathrm{d}r} - \hat{u}_{2\theta}\right) = 0,$$

$$\hat{p}_2 - \frac{2}{Re}\frac{\mathrm{d}\hat{u}_{2r}}{\mathrm{d}r} + \hat{q}_s\frac{\zeta D_2\xi}{D_2\xi + D_1\varepsilon_{r2}} + \hat{\eta}_2\left(\frac{1 - n^2 - k^2}{We} - \frac{\varepsilon_{r2}\zeta D_1(1 + k\xi)}{D_2\xi + D_1\varepsilon_{r2}}\right) = 0.$$

REFERENCES

Ash, R. L. & Khorrami, M. R. 1995 Vortex stability. In *Fluid Vortices* (ed. S. I. Green). Kluwer Academic Publishers.

Avital, E. 1995 Asymmetric instability of a viscid capillary jet in an inviscid media. *Phys. Fluids* **7**, 1162–1164.

Chen, X. P., Jia, L. B., Yin, X. Z., Cheng, J. S. & Lu J. 2005 Spraying modes in coaxial jet electrospray with outer driving liquid. *Phys. Fluids* **17**, 032101.

Chen, J. N. & Lin, S. P. 2002 Instability of an annular jet surrounded by a viscous gas in a pipe. *J. Fluid Mech.* **450**, 235–258.

Fong, H., Chun, I. & Reneker, D. H. 1999 Beaded nanofibers formed during electrospinning. *Polymer* **40**, 4585–4592.

Hartman, R. P. A., Brunner, D. J., Camelot, D. M. A., Marijnissen, J. C. M. & Scarlett, B. 2000 Jet break-up in electrohydrodynamic atomization in the cone-jet mode. *J. Aerosol. Sci.* **31**, 65–95.

Higuera, F. J. 2007 Stationary coaxial electrified jet of a dielectric liquid surrounded by a conductive liquid. *Phys. Fluids* **19**, 012102.

Li, F., Liu Z. Y., Yin, X. Y. & Yin, X. Z. 2007 Theoretical and experimental investigation on instability of a conducting liquid jet under a radial electric field. *Chin. Q. Mech.* **28**, 517–520.

Li, F., Yin, X. Y. & Yin, X. Z. 2008*a* Instability of a viscous coflowing jet in a radial electric field. *J. Fluid Mech.* **596**, 285–311.

Li, F., Yin, X. Y. & Yin, X. Z. 2008*b* Instability of a leaky dielectric coaxial jet in both axial and radial electric fields. *Phys. Rev.* E **78**, 036302.

Lin, S. P. 2003 *Breakup of Liquid Sheets and Jets*. Cambridge University Press.

López-Herrera, J. M., Barrero, A., López, A., Loscertales, I. G. & Márquez, M. 2003 Coaxial jets generated from electrified Taylor cones. Scaling laws. *J. Aerosol. Sci.* **34**, 535–552.

Loscertales, I. G., Barrero, A., Guerrero, I., Cortijo, R., Marquez, M. & Gañán-Calvo, A. M. 2002 Micro/nano encapsulation via electrified coaxial liquid jets. *Science* **295**, 1695–1698.

Melcher, J. R. & Taylor, G. I. 1969 Electrohydrodynamics: a review of the role of interfacial shear stresses. *Annu. Rev. Fluid Mech.* **1**, 111–146.

Mestel, A. J. 1996 Electrohydrodynamic stability of a highly viscous jet. *J. Fluid Mech.* **312**, 311–326.

Saville, D. A. 1997 Electrohydrodynamics: the Taylor–Melcher leaky dielectric model. *Annu. Rev. Fluid Mech.* **29**, 27–64.

Shen, J. & Li, X. 1996 Instability of an annular viscous liquid jet. *Acta Mech.* **114**, 167–183.

Son, P. H. & Ohba, K. 1998 Theoretical and experimental investigations on instability of an electrically charged liquid jet. *Intl J. Multiphase Flow* **24**, 605–615.

Sun, Z. C., Zussman, E., Yarin, A. L., Wendorff, J. H. & Greiner, A. 2003 Compound core-shell polymer nanofibers by co-electrospinning. *Adv. Mater.* **15**, 1929–1932.

Yu, J. H., Fridrikh, S. V. & Rutledge, G. C. 2004 Production of submicrometer diameter fibers by two-fluid electrospinning. *Adv. Mater.* **16**, 1562–1566.

Zuo, W., Zhu, M., Yang, W., Yu, H., Chen, Y. & Zhang, Y. 2005 Experimental study on relationship between jet instability and formation of beaded fibers during electrospinning. *Polym. Engng Sci.* **45**, 704–709.